Submitted and under review

Microscopic Analysis of Thin-Film Evaporation on Spherical Pore Surfaces

Kimia Montazeri[1], Hyoungsoon Lee[2], Yoonjin Won[1*]

[1] *Mechanical and Aerospace Engineering, University of California, Irvine*
Irvine, CA 92697, USA
[2] *School of Mechanical Engineering, Chung-Ang University, South Korea*
** Corresponding author email: won@uci.edu*

ABSTRACT

As electronic systems become miniaturized, it is crucial to implement optimal cooling technologies to dissipate high heat levels. Evaporation cooling for electronics systems has been considered one of the most promising approaches for meeting the demands of high-powered technologies by taking advantage of their latent heat. In this process, microscale or nanoscale features integrated into two-phase microfluidic cooling systems such as porous media dramatically increase the area of liquid-vapor interfaces where phonons translate thermal energy to fluid enthalpy. Therefore, the understanding of engineered features' effects on evaporation process is essential with the aim of enhancing evaporative heat transfer performance through structured surfaces. In this study, we investigate thin-film evaporation performance within crystalline pore surfaces by employing simulation models that examine solid-liquid contact lines and liquid-vapor interfaces. The simulation models compute detailed performance parameters including phase volume fraction, temperature, pressure profile, and evaporative mass flux as a function of location, allowing us to calculate local heat transfer performance parameters. Based on local heat transfer performances, we identify three evaporation regimes and quantify their contributions to the overall evaporation performance. Area-averaged heat transfer coefficients are compared for varying pore diameters and surface wettability. The insights from this parametric study will allow us to understand how evaporative heat transfer is related to the structural details of porous media to set a guideline for evaporating surface designs in modern electronics cooling.

KEY WORDS: copper invers opals, meniscus formation, thin-film evaporation, two-phase cooling

NOMENCLATURE

A	area, μm^2
CA	contact angle, ^{o}
c_p	specific heat, J/kg×K
d	diameter, μm
E	energy, J/kg
g	gravitational acceleration, m/s^2
h_{fg}	enthalpy of evaporation, J/kg
k	thermal conductivity, W/m×K
M	molar weight, kg/mol
$\dot{m}''$	mass flux, $kg/m^2 \times s$
P	pressure, Pa
q''	heat flux, W/m^2
Q	energy source, W/m^3
R	universal gas constant, J/mol×K
r	radius, μm
S	volumetric mass source, $kg/m^3 \times s$
T	temperature, K
t	flow time, s
u	velocity, m/s

Greek symbols

α	volume fraction
δ	thickness, μm
μ	viscosity, Pa×s
ρ	mass density, kg/m^3
σ	accommodation factor
ϕ	porosity

Subscripts

b	bottom
c	condensation
cell	cell
conv	convection
e	evaporation
eff	effective
IO	inverse opal
in	in
l	liquid
lv	liquid-vapor
pore	pore
s	solid
sat	saturation
sl	solid-liquid
v	vapor
via	via

1. INTRODUCTION

As electronic devices become smaller and more compact, their need for sophisticated disruptive thermal technologies increases concomitantly [1]. While current thermal management solutions using air cooling [2], single-phase liquid cooling [3], or thermoelectric cooling schemes [4] cannot meet the demands of high-performance electronics, two-phase cooling devices offer a promising approach over conventional single-phase cooling architectures by utilizing latent heat during phase change process [5]. In particular, two-phase cooling devices integrating porous materials show a significant improvement in evaporation regime because of their favorable combination of conduction and convection properties as well as enormous interfacial area [6-7]. Porous materials provide conduction pathways through their solid fraction and enable efficient convection transport between solid and liquid phases through their large specific surface area. Therefore, the implementation of porous materials into recent microfluidic heat exchangers such as vapor chambers and heat pipes [8] is suggested to push toward the fundamental limits of evaporative cooling.

Although new porous materials show a promising framework, still the understanding between the porous materials' structural details and their evaporation performance is lacking, which is essential for the optimum design of porous structures. Various design challenges are closely related to the contributions of the different transport mechanisms; for example, liquid transport by capillary pumping within a porous medium competes with the viscous resistance associated with small pores [9-11]; thermal conductivity generally decreases with porosity while hydraulic permeability increases; and evaporation benefits from engineered materials to control the shape of the meniscus and to minimize diffusion lengths through the often-insulating liquid phase [12]. Most current design challenges can be carefully investigated through theoretical parametric studies that can identify the critical material parameters to engineer optimized evaporative cooling surfaces.

Recently, thin-film performances using nanoporous membranes [12,13] and microfabricated pin fin arrays [14] were experimentally investigated to explore the effects of morphological parameters (e.g., pore size, wick depth, and heated area) on evaporative heat transfer [15]. However, the understanding from previous experiments has been limited due to the structural material choices and geometric parameters that are dictated by their fabrication methods [12], which requires a theoretical approach to convey a systematic parametric study. Furthermore, if evaporating surfaces are integrated with force convection flows, it is difficult to understand the flow effects of forced convection on evaporation without additional aids from computational models. [16]. Therefore, it is imperative to develop computational simulation models such as computational fluid dynamics (CFD) to explore a wide range of parameters to complete the design guidelines or to carefully investigate the physics that are difficult to experimentally measure, specially, with the presence of nanoscale structures.

In this context, there have been substantial efforts to study phase change processes such as boiling [17-18], evaporation [19-24], and condensation [25-26] by implementing phase change theory into CFD simulation tools [27]. The majority of wicking surfaces in prior studies included packed spheres [28-30], wire meshes [30], grooves [31-35], and sintered powder wicks [36] on order of submillimeter [37]. The reported heat transfer coefficients in these studies are much lower than the theoretical limit based on the kinetic theory because the effective thin-film area occupies only a small portion of the meniscus (approximately 20%), while most evaporative mass flux occurs through this small thin-film evaporating region [12, 38-40]. Therefore, the series of previous work motivate to examine local evaporation performance parameters of porous structure, in particular, on order of tens of micrometer with the aim of investigating the role of structural characteristic lengths in determining evaporation performance.

To address such challenges, this study demonstrates a comprehensive analysis of the microstructures' effects on meniscus formation and thereby thin-film evaporation by employing highly-ordered porous materials. Here, we examine a wide range of morphological parameters by computing both solid-liquid contact lines and liquid-vapor interfaces in order to provide a set of guidelines to optimize porous structures. The fundamental understanding from this study will allow us to pave the way to better design evaporating surfaces to solve thermal challenges in modern electronics devices.

2. Methods

2.1. Microstructure Topology using Inverse Opals

This work investigates evaporative heat transfer parameters using crystalline porous structure that possesses structural regularity in order to understand the morphological effects on evaporation performance. As an example of crystalline porous structure, this work employs copper inverse opals (IOs) (Fig. 1(a)), which are inverted structures of self-assembled sacrificial spheres forming a close-packed configuration [41]. Here, the sacrificial spheres' diameter will decide pore diameter d_{pore} ranging from 50 nm to 20 μm; After the sacrificial template removal, the necks between adjacent spheres in the template will become a "via" (that is interconnected windows between the pores), enabling high fluid accessibility with a large specific surface area. The manufacturing process of IOs demonstrates highly-ordered porous materials with a precise control of morphological parameters by modulating sacrificial sphere size, annealing process, and deposition material. The combination of periodicity and regularity of IOs allows us to predict the IOs' transport physical parameters by developing a unit cell model with symmetry boundary conditions (Fig. 1(b)). In the past study, we have calculated the IOs' porosity and permeability based on the assumption of IOs' face-centered configuration (FCC), which shows a good agreement with experimental measurements [42].

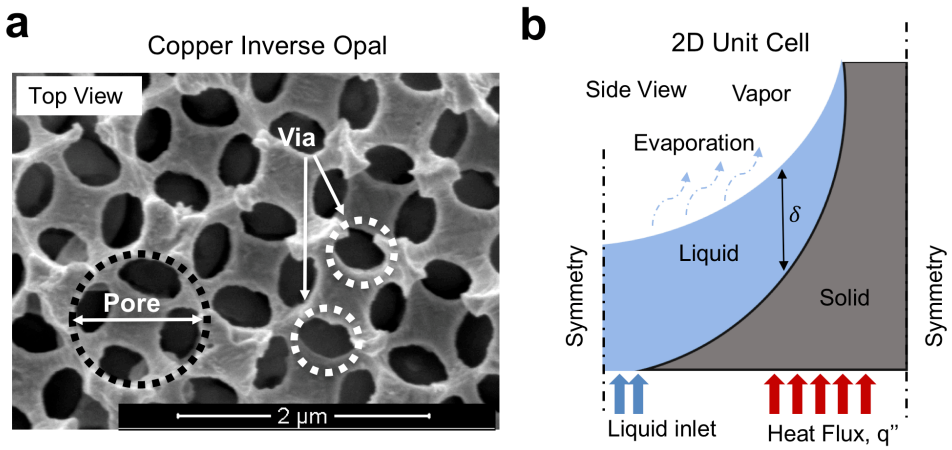

Figure 1. (1.5 column) Structural regularity and periodicity of copper inverse opals. (a) Representative scanning electronic microscope image of copper inverse opal shows face-centered configuration. The combined interconnectivity and periodicity of the pores provide liquid flow paths through the porous structure and enables a unit cell approach. (b) Schematic of the IO's 2D unit cell shows symmetry boundary conditions. Liquid inlet with v = 0 m/s is introduced from the bottom liquid cells while a constant heat flux q'' is added to the bottom solid cells. In addition, the IOs' spherical concave shape helps to minimize meniscus thickness and to enhance evaporating areas.

2.2. Liquid Meniscus Computation

We track how liquid-vapor interfaces evolve within a spherical concave pore representing a unit cell of copper IO structures through Surface Evolver [43]. Surface Evolver solves for liquid-vapor interfaces associated with surface forces, gravitational force, and other constraints (i.e., contact angle and liquid volume fraction) by calculating total energy for different conditions. Gradient descent method, a first-order iterative optimization algorithm, is used to find local minimum of total energy of interfacial surfaces. By repeating gradient descent iterations, the shape of liquid-vapor interfaces is obtained possessing the minimum total energy in which the system reaches to an equilibrium state. The liquid meniscus thickness for different contact angles inside an IO pore with a constant liquid volume fraction (32.5% of the IO pore) is shown in Fig. 2 where the normalize thickness is defined as a vertical distance between liquid-vapor and solid-liquid interfaces in an IO pore over the pore radius (see the vertical arrow in Fig. 1(b)). As indicated, the liquid with smaller contact angles is prone to wet the IO pore surface, enabling extreme thin liquid film over a larger area whereas large contact angles provide thicker liquid film, occupying only a small portion of the IO pore surface. The meniscus shapes obtained from Surface Evolver are then imported to SolidWorks for post-processing, ANSYS Meshing and Fluent for mesh generation and CFD calculations, respectively.

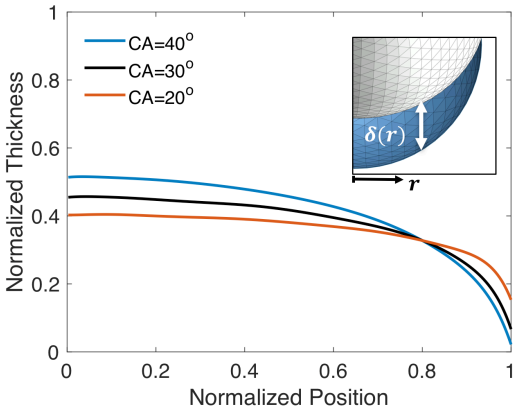

Figure 2. (single column) Meniscus thickness as a function of position in the *r*-direction in normalized coordinates. Normalized thickness is calculated based on the ratio between a vertical distance between liquid-vapor and solid-liquid lines and the pore radius. As a contact angle decreases, the thickness at the center decreases (where normalized $r = 0$), possessing larger extended meniscus. (Inset) Capture from Surface Evolver shows the interface between liquid (blue) and vapor (gray) phases in an IO pore (white).

3. Mathematical Model

3.1. Governing Equations

3.1.1 Volume of Fluid Method

Once the meniscus shapes are imported to ANSYS Fluent, volume of fluid (VOF) method identifies different phases to track liquid-vapor interfaces in the computational domain by assuming two phases are not interpenetrating each other. In this VOF method, the value of 1 indicates that the cell is filled with primary phase (liquid in this case) while the value of 0 indicates the cell is occupied by other than primary phase. Cells with the values between 0 and 1 represent the presence of two-phase interfaces as Fig. 3 shows a representative phase contour. Afterwards, mass conservation equations are solved separately for liquid and vapor phases:

$$\frac{\partial}{\partial t}(\alpha_l \rho_l) + \nabla \cdot (\alpha_l \rho_l \overrightarrow{u_l}) = S_l \tag{1}$$

$$\frac{\partial}{\partial t}(\alpha_v \rho_v) + \nabla \cdot (\alpha_v \rho_v \overrightarrow{u_v}) = S_v \tag{2}$$

where α is the volume fraction, ρ is the density, u is the velocity vector, and S is the volumetric mass source term that accounts for mass transfer between the phases. Subscripts l and v represent liquid and vapor, respectively. A single set of momentum and energy equations is solved for the entire domain:

$$\frac{\partial(\rho \vec{u})}{\partial t} + \nabla \cdot (\rho \vec{u}\vec{u}) = -\nabla P + \nabla \cdot [\mu(\nabla \vec{u} + \nabla \vec{u}^T)] + \rho \vec{g} + \vec{F} \tag{3}$$

$$\frac{\partial(\rho E)}{\partial t} + \nabla \cdot \left(\vec{u}(\rho E + P)\right) = \nabla \cdot (k \nabla T) + Q \tag{4}$$

where Q is the energy source term, and E is the energy, which can be defined as the phase-averaged value:

$$E = \frac{\alpha_l \rho_l E_l + \alpha_v \rho_v E_v}{\alpha_l \rho_l + \alpha_v \rho_v} \tag{5}$$

The properties used in momentum and energy equations are defined as effective values for the combined phase and are obtained based on the volume fractions of each phase:

$$\rho_{eff} = \alpha_l \rho_l + \alpha_v \rho_v \tag{6}$$

$$\mu_{eff} = \alpha_l \mu_l + \alpha_v \mu_v \tag{7}$$

$$k_{eff} = \alpha_l k_l + \alpha_v k_v \tag{8}$$

where μ is the viscosity, and k is thermal conductivity.

3.1.2. Phase Change at Interfaces

The interfacial mass and energy transfer is considered by adding appropriate volumetric mass source term S and energy source term Q to continuity and energy equations in Eq. (1,2,4), respectively, through the use of user defined functions (UDFs). The volumetric mass source term imposed on the liquid phase S_l has a negative value because of the evaporative mass from liquid to vapor phase. Therefore, $S_l = -S_v = -\dot{m}'' |\nabla \alpha_v|$ based on Schrage model [44], where $|\nabla \alpha_v|$ is the interfacial area over the volume within one computational cell as expressed in this equation [42]:

$$|\nabla \alpha_v| = \frac{1}{V} \int |\nabla \alpha_v| \, dV = \frac{A_{lv,cell}}{V_{cell}} \tag{9}$$

The values of $|\nabla \alpha_v|$ are obtained by using a user defined function to calculate evaporative mass fluxes. Then, an energy source term $Q = h_{fg} S_l$ is added to the energy equation at liquid and vapor interfaces in order to account for enthalpy difference between liquid and vapor during the phase change. Schrage theory [44] provides the correlation between the mass flux and thermofluidic profiles in the two-phase system [26,46]:

$$\dot{m}'' = \frac{2}{2 - \sigma_c} \sqrt{\frac{M}{2\pi R}} \left[\frac{\sigma_c P_v}{\sqrt{T_v}} - \frac{\sigma_e P_l}{\sqrt{T_l}} \right] \tag{10}$$

where R is the universal gas constant (8.314 J/mol×K), and M is the molar weight (0.018 kg/mol for water). In Eq. (10), the accommodation factor σ is the fraction of molecules transferred due to the phase change while subscripts c and e dictate condensation and evaporation. In the most of previous studies, the accommodation factors for condensation σ_c and evaporation σ_e are treated as an identical value σ [45]. The value of σ=1 means all the molecules at the interface line changes their phases. Often, the values of larger than 0.1 are suggested for dynamic surfaces (i.e., boiling), and the values of smaller than 0.1 are suggested for static surfaces (i.e., condensation or evaporating surfaces) [46]. Tanasawa's model assumes that there is a small temperature jump between the liquid-vapor interface and vapor with a linear correlation between those two temperatures [47], and simplifies Eq. (10):

$$\dot{m}'' = \frac{2\sigma}{2 - \sigma} \sqrt{\frac{M}{2\pi R}} \frac{\rho_v h_{fg} (T - T_{sat})}{T_{sat}^{\frac{3}{2}}} \tag{11}$$

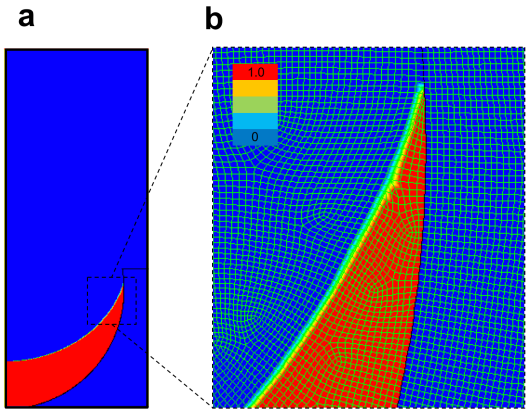

Figure 3. (single column) Phase contour representing liquid and vapor phases on a solid surface. (a) In this contour, red with the value of 1 indicates liquid phase while blue with the value of 0 dictates other phases. The cells with the values between 0 and 1 indicate vapor-liquid interfaces. (b) Close-up view of phase contour shows the detailed mesh in different phases and at interfaces. Thin liquid film near the solid surface is shown.

3.2. Numerical Simulation

Based on the numerical correlations from Eq. (1-10), transient thin-film evaporation models are developed to calculate thermofluidic performance parameters. First, a two-dimensional (2D) unit cell from Fig. 4(a) is considered by using incompressible and laminar flow with a pressure based solver. Then, the simulation models use semi-implicit method for pressure linked equations (SIMPLE scheme) [48], least square cell based formulation for gradient spatial discretization, and PRESTO! scheme [49] for pressure discretization. In the models, VOF method computes different phases with explicit formulation and implicit body forces while volume fraction cutoff and Courant number are the default values of 10^{-6} and 0.25, respectively. High resolution interface-capturing (modified HRIC) [50] discretizes the volume fraction where its computational expense is smaller than Geo-Reconstruct scheme. Momentum and energy equations are discretized using second order upwind scheme [51]. Continuum surface force (CSF) model [52] helps to maintain constant contact angles during evaporation process (simulation details are listed in Table S1).

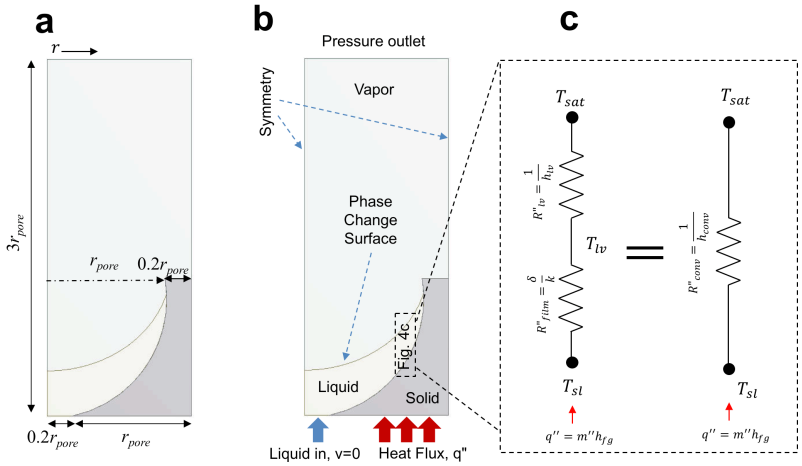

Figure 4. (1.5 column) Computational unit cell of copper inverse opal showing geometrical details and boundary conditions. (a) Unit cell dimensions are indicated where the via is defined as 20% of a pore diameter. (b) Boundary conditions include liquid in and a constant heat flux in from the bottom surface as well as symmetry conditions due to the periodicity of the IOs. Liquid to vapor phase change occurs only at the interfacial regions. (c) Thermal circuits represent the film resistance and interfacial transport resistance in series (left), which is equivalent to the convective heat transfer resistance (right) based on the one-dimensional conduction assumption.

3.3. Geometry, Boundary Conditions, and Material Properties

This work examines a 2D IO unit cell for varying pore diameters from 10 μm to 20 μm. All the geometrical values are expressed as a function of pore diameter. Thereby, once the pore diameter increases, other geometrical values will increase in relation to the pore diameter. Detailed dimension information of unit cell is indicated in Fig. 4(a). As boundary conditions for a 2D IO unit cell (with a $1.2r_{pore}$ in width and a $3r_{pore}$ in height) are illustrated in Fig. 4(b), the working fluid is introduced through a via with an inlet velocity of 0 m/s at a constant temperature where the radius of the via is $r_{via} = 0.2r_{pore}$. The ratio between via and pore sizes gives us a constant porosity of 78%. A heat flux of q'' = 100 W/cm^2 is applied to the solid portion of the bottom surface. The liquid in the inlet has a constant temperature of 373 K, and solid phase is initially superheated at 380 K. We can track the recession of interface as the water evaporates inside the pore. Symmetric boundary conditions are applied at the sides because of the periodic structure of IOs**.** Pressure outlet boundary condition is used at the top surface, and the temperature at the outlet is equal to the vapor saturation temperature T_{sat}. In all simulation models, the working fluid and solid material are water and copper, respectively. The thermophysical properties of water and copper are listed in Table S2 and S3 where saturation temperature and enthalpy of evaporation are reported at P = 1 atm.

4. Results

We perform a parametric study of evaporation performance by testing various pore diameters of copper IO cell ranging from 10 to 20 μm and contact angles of 20°-40°. The computational models directly provide thermofluidic parameters such as spatial and temporal temperatures, pressures, velocity profiles, and evaporative mass fluxes, allowing us to compute heat transfer coefficients. Here, the liquid-vapor interface is defined as the cells that have a volume fraction of 0.5. Since the interface temperature gets stabilized in 10^{-5}s after the initialization for all the cases, we select 10^{-5}s as a flow time for this study.

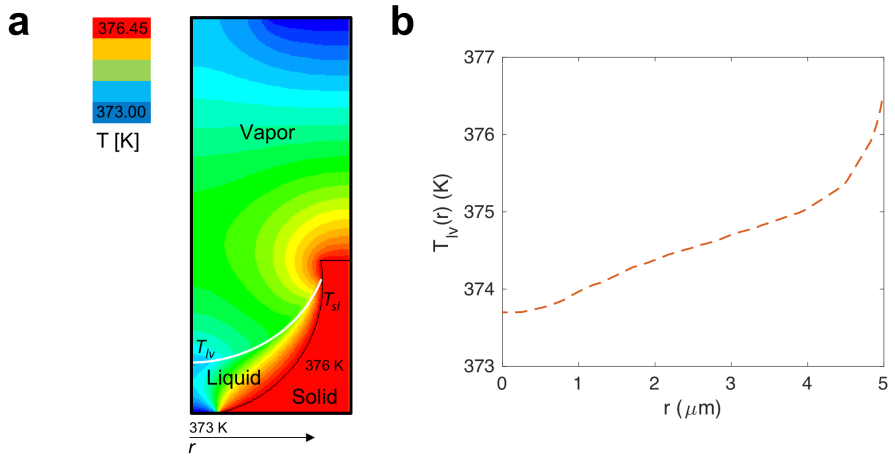

Figure 5. (1.5 column) Temperature profile in the liquid, vapor, and solid domains under evaporation regimes where d_{pore} = 10 μm and CA = 20°. (a) Temperature contour shows the increase in temperature at the wall along the interface. (b) Temperature profile along the liquid-vapor interface is plotted against the r-axis, which confirms lower temperature at the inlet and higher temperature near the wall at r = 5 μm.

4.1. Local Evaporative Mass Flux

The computational simulation models calculate local evaporative mass flux using the simplified version of Schrage model in Eq. (10). The examples of the cases of d_{pore} = 10 μm and d_{pore} = 20 μm are plotted in Fig. S1(a) and (b).

4.2. Temperature Profiles

Fig. 5(a) shows the temperature contour in the liquid, vapor, and solid domains of the evaporating meniscus where d_{pore} = 10 μm and CA = 20°. After t = 10^{-5} s, the detailed temperature profile $T_{lv}(r)$ along the liquid and vapor interface is plotted in Fig. 5(b) where the liquid volume fraction is 0.5. As indicated, the temperature T_{lv} is minimum at the center of the pore (at r = 0 μm) that is influenced by the liquid inlet with a constant temperature of 373 K. The temperature T_{lv} at r = 5 μm near the wall is shown to be much higher because of lower conduction resistance, which is proportional to liquid film thickness based on Fourier's law.

In the solid region of the unit cell, the conduction is a dominant heat transfer mode. Therefore, the temperature deviation is relatively small (compared to temperature profiles in the liquid or vapor regions) as the copper has a high thermal conductivity. The local temperature information $T_{sl}(r)$ will be plugged in Eq. (11) to calculate the corresponding local heat transfer coefficient. The area-averaged solid temperatures T_{sl} for different pore diameters and contact angles are compared in Fig. 6. In this plot, as the pore diameter increases, the average temperature increases as well. This might be an evidence of efficient evaporation performance for smaller pore diameters.

4.3. Computation of Local Heat Transfer Coefficient

To characterize the evaporation heat transfer performance in the copper IO cell, we assume one-dimensional (1D) heat transfer [53] from the solid surface to the liquid (phonons and electrons in solid phase translate thermal energy to fluid enthalpy) and from the liquid to the evaporating surface (thermal energy is transferred by both conduction and advection through the thin-film liquid regime and further translated through to the vapor regime via thin-film evaporation). Such transport physics with 1D assumption can be represented by the thermal resistances in series in Fig. 4(c) such that the input heat $q" = h_{conv}(r)(T_{sl}(r) - T_{sat})$ is assumed to be equal to the heat transferred from the interface $q" = \dot{m}"(r)h_{fg}$. Therefore, the local heat transfer coefficient can be calculated as:

$$h_{conv}(r) = \frac{\dot{m}"(r)h_{fg}}{T_{sl}(r) - T_{sat}} \tag{12}$$

by using local evaporative mass flux $\dot{m}"$(r) and local solid-liquid temperature $T_{sl}(r)$. In Fig. 4(c), the combined thin-film resistance and evaporation resistance can be defined as the local convective thermal resistance $R_{conv}(r)$:

$$R_{conv}(r) = \frac{1}{h_{conv}(r)A} \tag{13}$$

where A is the interface area between solid and liquid phases.

In this work, a local convective heat transfer coefficient along the interface is computed as a function of radius, which will allow us to understand the local evaporative heat transfer performance related to local meniscus thickness. Fig. 7 shows the representative $h_{conv}(r)$ profiles using copper IOs with d_{pore} = 10 μm and 20 μm. In this plot, a maximum h_{conv} at the wall reaches to the values of 700 kW/m^2×K in the thin-film region for both cases.

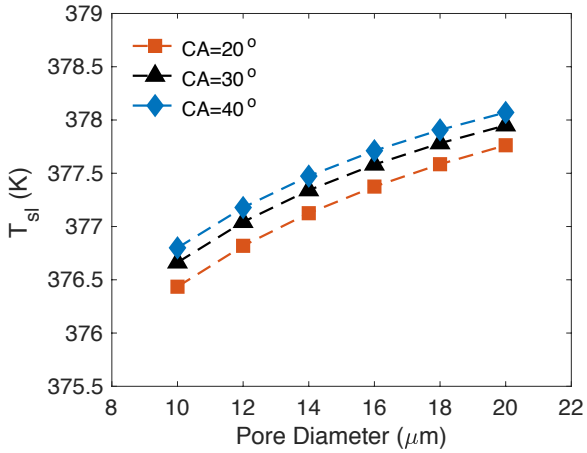

Figure 6. (single column) Area-averaged temperature of solid-liquid contact lines for varying pore diameters and CA = 20°. As the pore diameter increases, the solid temperature increases, indicating the decrease in evaporation rates.

5. Discussion

This study reveals crystalline IOs' role in improving thin-film evaporation related to meniscus shapes by computing local and average heat transfer coefficients. Local heat transfer coefficients are calculated based on the evaporative mass flux and the difference between solid temperature and saturation temperature, and they are used to identify different evaporation regimes along the interface. The area-averaged heat transfer coefficients are computed to compare overall evaporative heat transfer performance for varying cases.

5.1. Evaporation Regime Identification

Based on Schrage model and Eq. (11), local evaporation performance parameters are plotted as a function of location in Fig. 7 and Fig. S1. In these plots, the local evaporative mass flux as well as local heat transfer coefficients are roughly inversely proportional to the local meniscus thickness. Based on these plots, three main evaporation regimes can be identified as: high-evaporating regime, evaporating regime, and non-effective regime as a function of the radial location as illustrated in Fig. 7. (1) The high-evaporating regime (0.9 $r_{pore} < r < r_{pore}$), most efficient evaporating regime, occurs near the wall where a sudden decrease in thin-film thickness is observed. Therefore, the high-evaporating regime occupies only a small portion of the thin meniscus, but the large portion of evaporative mass occurs through this small region, which is called the "contribution" of high-evaporating regime. Here, the contribution percentage is defined as the ratio of evaporative mass transfer through the thin-film area and the total mass transfer through the entire interface:

$$Contribution = \frac{\int_{0.9r_{pore}}^{r_{pore}} \dot{m}"dr}{\int_{0}^{r_{pore}} \dot{m}"dr} \tag{14}$$

In Fig. 8, the contribution of high-evaporating regime to the total evaporative heat flux is plotted for varying pore diameters, which ranges from 35% to 50% as pore diameter increases. Smaller pores show smaller contributions, indicating the creation of efficient and uniform evaporation over the pore surface. However, larger pores show larger contributions, which means the evaporation of larger pores is mostly dominated by the presence of high-evaporating regime. (2) The evaporating regime, which is the transition

between the high-evaporating regime and non-effective regime, occupies a large portion of the meniscus. (3) In the non-effective regime (if a local evaporative mass flux is less than 1% of the maximum evaporative mass flux at the wall), the local temperature profile is directly affected by the inlet temperature, which is often lower than the saturation temperature. Thereby, evaporation phase changes happen at a very small rate. Note that nanoscale non-evaporating regimes near the wall because of molecular-level forces between solid and liquid molecules are reported elsewhere but they are not studied in this microscale analysis [54].

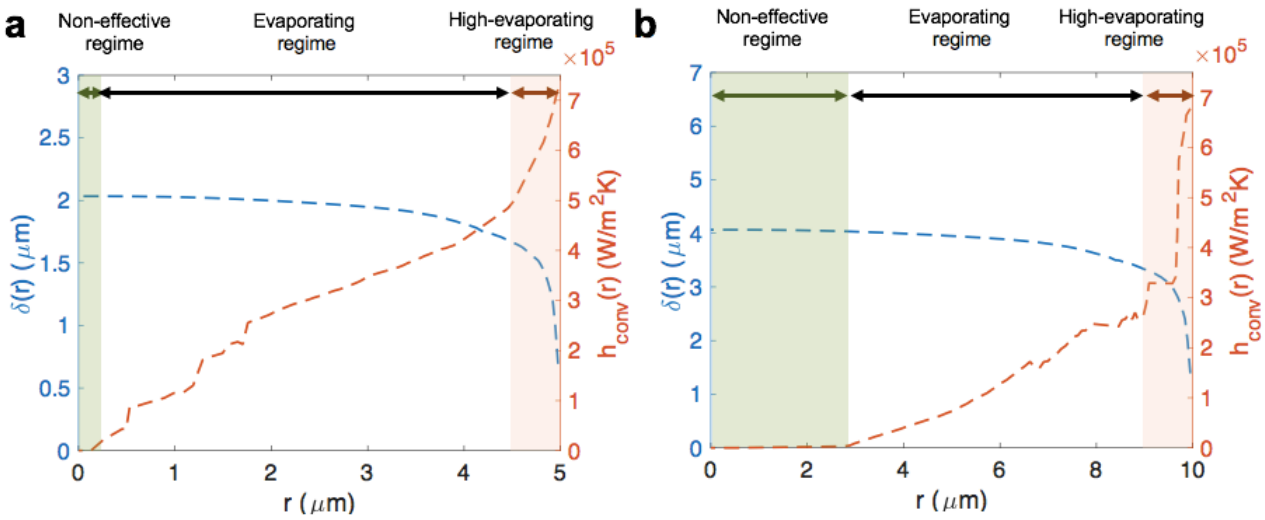

Figure 7. (double column) Local heat transfer parameters after simulating for a flow time of $t = 10^{-5}$ s. Local meniscus thickness and heat transfer coefficients along the liquid-vapor interface (a) for the case of $d_{pore} = 10$ μm and (b) $d_{pore} = 20$ μm where the contact angle is 20°. Based on these local plots, the evaporation regimes are identified as high-evaporating regime ($0.9\, r_{pore} < r < r_{pore}$), evaporating regime, and non-effective regime.

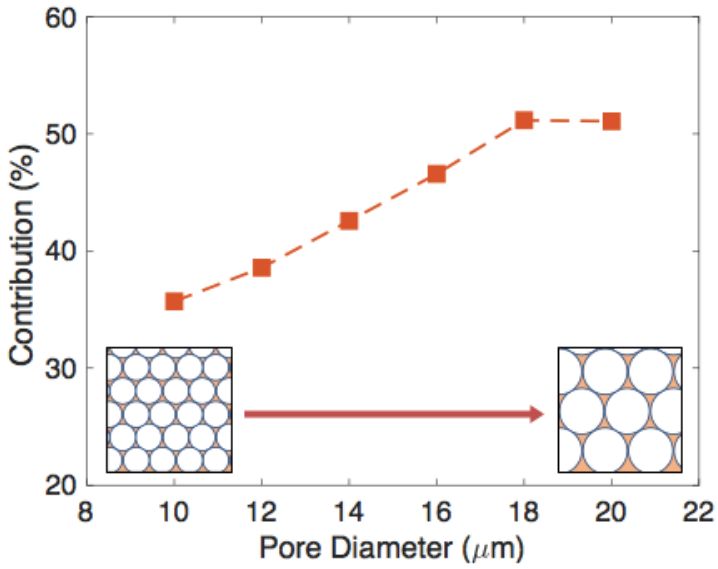

Figure 8. (single column) Contribution of high-evaporating regime to the total evaporative heat flux for varying pore diameters, which ranges from 35% to 50% as pore diameter increases. Smaller pores show smaller contributions, indicating the creation of efficient and stable evaporation while the evaporation of larger pores is dominated by high-evaporating regime only.

5.2. Effects of Pore Diameters on Evaporation

We perform a parametric study of evaporation performance by testing different pore diameters ranging from 10 to 20 μm. This range of pore diameter is selected based on the error analysis (See Section 6.2 for details). Area-averaged evaporative mass flux, evaporative heat flux, and convective heat transfer coefficients as a function of pore diameter are calculated to understand their effects on overall evaporation phenomena in Fig. 9 and Fig. S2. In these plots, by decreasing the pore diameter by a factor of 2, area-averaged evaporative mass flux increases by 10% - 33% and area-averaged convective heat transfer coefficient increases by 70% for CA = 20°, 85% for CA = 30°, and 120% for CA = 40°, respectively. This can be attributed to the presence of different portions of non-effective regimes for different pore diameters as compared in Fig. 7. For example, smaller pore diameter of d_{pore} = 10 μm possesses a small portion of non-effective regime (< 5%) while larger pore diameter of d_{pore} = 20 μm shows a large portion of non-effective regime (25%) as indicated in local regime plots, which helps small pores to lead to more efficient evaporation in overall. This investigation shows that attaining small characteristic lengths is critical to enhance evaporation performance using crystalline porous structures.

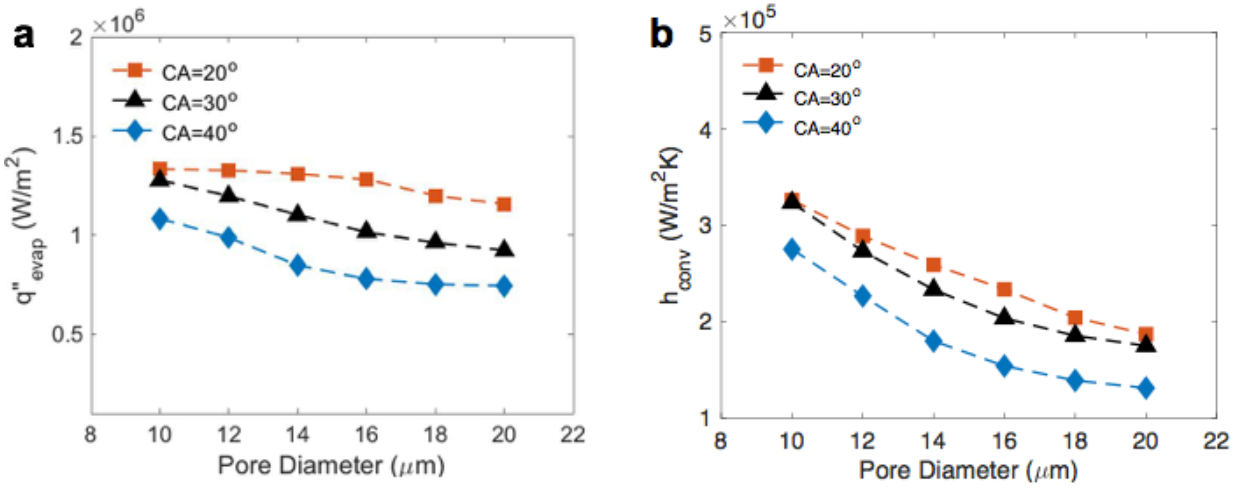

Figure 9. (double column) Area-averaged evaporation performance values for varying pore diameters and contact angles. (a) Area-averaged heat flux and (b) heat transfer coefficients are plotted for different cases. The changes in pore diameters and contact angles will significantly affect the corresponding heat transfer coefficients.

5.3. Role of Contact Angles in Evaporation

In addition to the pore diameters, another important parameter to determine overall evaporation performance is surface wettability, which can be quantified with a contact angle via the Young equation. Often, surface wettability can be controlled by surface engineering methods that modulate both surface roughness and chemistry. In order to account for such surface engineering effects, we vary contact angles between the solid wall and liquid inside the pore for our simulation models, which are ranging from 20° to 40°. The contact angle values are directly plugged in Surface Evolver to determine the liquid film thickness first and then their thermofluidic properties are calculated using the CFD models (as explained in section 3 and 4). Surface wettability plays key roles in determining evaporation performance parameters: (1) The liquid with smaller contact angles is prone to wet an IO surface, allowing evaporating surfaces to possess enormous surface areas; (2) The liquid with smaller contact angles minimizes the thickness deviation along the interface, enabling more stable evaporating performance over the entire system; and (3) While area-averaged heat transfer coefficient increases as the pore diameter decreases, the liquid with smaller CAs is relatively less sensitive to the changes in pore diameters (see Section 5.2). As a result, as contact angle decreases from 40° to 20°, the improvements in evaporative mass flux increases is reported as 20% - 60%.

6. Validation of Computational Model

6.1. Mesh independence study

Courant number indicates the numerical correlation among the computational cell size Δx, the transient time step Δt, and the velocity of the liquid flowing inside the cell v, as $C = v\Delta T/\Delta x$. Thereby, Courant number explains how much information propagates through a computational cell in each time step and directly affects the convergence quality of the calculations. Using inappropriate values of Courant number results in data transfer through more than one cell at each time step, causing the calculation to be unstable and unphysical [51]. Considering the microscale computational domain of a single unit cell, to maintain the Courant number within convergence criteria (Courant number is usually smaller than 1 in VOF method), it is required to use the values of time step of 10^{-9} s. Based on this time step, it is essential to choose a mesh size to reach a reasonable calculation time for the simulation process.

To confirm the independency of the results from the computational mesh of this work, we test three different mesh sizes by performing numerical simulation for each of them. The number of cells in each of the discretized geometries are 9151, 36579, and 145019. The average mesh size for each mesh is 0.112, 0.054, and 0.024 μm, respectively. Temperature profiles along the liquid-vapor interface and solid-liquid contact line are calculated for each of the meshes, as listed in Table S4 (in Supplementary Information). The percentage differences between the average wall temperature and interface temperature for each pair are calculated in Table S5. Since the deviations between the results are negligible, for a proper cost-effective balance, we choose mesh 2 as the suitable discretized domain for simulations. The calculation time of using mesh 2 is decreased by factor of 2 compared to mesh 3 and takes several days to converge.

6.2. Energy balance study

We employ energy balance calculations in order to validate the evaporation models developed in this work for various pore diameters in the range of 2 - 20 μm and contact angles of 20°, 30°, and 40°. Total energy added to the unit-cell (through a heat flux from the bottom surface) Q_{in} is used to increase the internal energy of liquid Q_l and solid phase Q_s (that are represented by sensible heats of the system) and to promote evaporation phenomena at the liquid-vapor interfaces Q_e (by utilizing latent heat). To represent such correlation, energy balance equation can be expressed as:

$$Q_{in} = Q_s + Q_l + Q_e \tag{15}$$

The total energy to the system with a given heat flux is:

$$Q_{in} = q" A_b t \tag{16}$$

Each energy component is defined as:

$$Q_s = \rho_s V_s c_{p_s} \Delta T_s \tag{17}$$

$$Q_l = \rho_l V_l c_{p_l} \Delta T_l \tag{18}$$

$$Q_e = \dot{m}" h_{fg} A_{lv} t \tag{19}$$

where t is the flow time, h_{fg} is the latent heat of evaporation, c_p is the specific heat, and ΔT is the temperature difference between initial and final states. A_{lv} and A_b show the liquid-vapor interface and bottom surface area, respectively. The subscripts s and l represent solid and liquid, respectively. Computational error is defined as the difference between the energy input and output divided by the total heat added to the system, thereby $Error = (Q_{in} - (Q_s + Q_l + Q_e))/Q_{in}$. Such computational error is calculated and reported for varying pore diameters in Fig. 10. Based on this analysis, the error significantly increases as pore diameters become smaller meanwhile the error is shown to be consistently smaller than 40% for large pores (where $d_{pore} > 10$ μm). The energy balance calculation indicates that our CFD models in this study are valid to account for microscale evaporation process if the pore diameter is larger than 10 μm. Therefore, all the calculations in this range have been reported in this study.

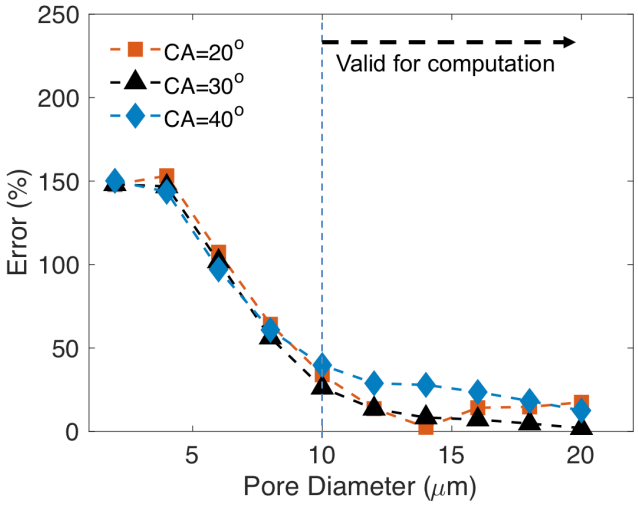

Figure 10. (single column) Energy balance calculation error reported for contact angles of 20°, 30°, and 40° and pore diameters ranging from 2 to 20 μm. The error is defined as the normalized difference between the energy input to the system and output from the system considering the evaporation rates obtained from simulation. It is observed that for diameters smaller than 10 μm. the error of calculations is significantly high. Therefore, we study the evaporation phenomena for diameters in the range of 10 to 20 μm.

6.3 Limitation of CFD models.

CFD computations have been challenging since phase change models rely dominantly on the rough estimation of empirical values (i.e., accommodation factors [52]). This work uses the value of 0.1 for accommodation factor, which is widely used in previous literatures that observed evaporation phenomena [53]. Furthermore, CFD computations are suitable for microscale systems but not ideal for nanoscale calculations whereas atomistic-level calculations are capable of calculating individual particle behaviors and their interactions based on numerical algorithms that account for interatomic forces between particles. For example, as the pore diameter decreases down to 1 μm, the meniscus thickness becomes on the order of nanometers. In this case, the atomistic-level calculations that account for intermolecular forces between water and copper molecules might be more critical and should be considered. For example, disjoining pressure, the excess pressure required for the evaporation at the thin-film region due to presence of solid-liquid interactions, is significant in the small-scale evaporation [11,35]. However, the effects of disjoining pressure on the suppression of evaporation cannot be considered in the present work without considering intermolecular forces on the thin-film region on the evaporation process. Furthermore, interfacial temperature jumps cannot always be neglected in microscale simulations. Therefore, in order to capture more complex phase change physics at interfaces, the study of atomistic-level calculations might be considered as a follow up study.

Conclusion

This study investigates the effects of pore surfaces on meniscus formation and evaporation parameters by computing both solid-liquid contact lines and liquid-vapor interfaces with the aim of understanding evaporation through the use of a crystalline porous structure called inverse opal. Here, a liquid meniscus shape is defined based on the minimum total surface free energy for a given intrinsic contact angle, which is later imported as an initial condition for two-phase calculations. The two-phase models compute transient thermofluidic properties such as local temperature, pressure, phase volume fractions, and mass flux by tracking liquid-vapor interface changes, allowing us to evaluate local heat transfer coefficients along the interface for varying cases. The local convective heat transfer coefficients increase as the meniscus thickness decreases, possessing the maximum value of 700 $kW/m^2 \times K$ near the wall. This analysis identifies how high-evaporating regimes occupying a small portion of the overall interface area dominate the total evaporation rate. Then, area-averaged convective heat transfer coefficients are correlated with pore diameters and contact angles. The decrease in the pore diameter from 20 to 10 μm results in a 70% - 120% improvement in heat transfer coefficient while the decrease in the contact angle from 40° to 20° leads to a 20% - 60% improvement in evaporative heat transfer coefficient. In this study, we have investigated a wide range of morphological parameters to systemically provide the parametric study related to evaporation performance, suggesting the design of smaller pores with desirable surface engineering

that create hydrophilic surfaces. The fundamental insights from this study will enable a rational design of evaporating surfaces to address thermal challenges in many applications.

Acknowledgement

This work was sponsored by the National Science Foundation (NSF), (CBET-TTP 1643347, Dr. Jose Lage, the Program Director, Thermal Transport Processes) and the National Research Foundation of Korea (NRF) grant funded by the Korea government (Ministry of Science, ICT & Future Planning) (No. 2017R1C1B5017566). K.M. is thankful for the financial support from the UCI Mechanical and Aerospace Engineering Department Graduate Fellowship.

References

[1] McGlen, R.J., Jachuck, R. and Lin, S., 2004. Integrated thermal management techniques for high power electronic devices. *Applied thermal engineering*, 24(8), pp.1143-1156. https://doi.org/10.1016/j.applthermaleng.2003.12.029

[2] Zhang, H.Y., Pinjala, D. and Teo, P.S., 2003, December. Thermal management of high power dissipation electronic packages: From air cooling to liquid cooling. In Electronics Packaging Technology, *2003 5th Conference (EPTC 2003)* (pp. 620-625). IEEE. https://doi.org/10.1109/EPTC.2003.1271593

[3] Heydari, A., Sun Microsystems, Inc., 2007. Multiple component field-replaceable active integrated liquid pump heat sink module for thermal management of electronic components. *U.S. Patent 7*,219,714.

[4] Vandersande, J.W. and Fleurial, J.P., 1996, March. Thermal management of power electronics using thermoelectric coolers. In Thermoelectrics, 1996., *Fifteenth International Conference* on (pp. 252-255). IEEE. http://dx.doi.org/10.1109/ICT.1996.553311

[5] Carey, V.P., 1992. Liquid-vapor phase-change phenomena.

[6] Richards, L.A., 1931. Capillary conduction of liquids through porous mediums. *Physics*, 1(5), pp.318-333.

[7] Palko, J. W., Lee, H., Zhang, C., Dusseault, T. J., Maitra, T., Won, Y., Agonafer, D. D., Moss, J., Houshmand, F., Rong, G., Wilbur, J. D., Rockosi, D., Mykyta, I., Resler, D., Altman, D., Asheghi, M., Santiago, J. G., and Goodson, K. E., (2017) Extreme Convective Boiling from Template-Fabricated Microporous Copper on Laser-Etched Diamond, *Advanced Functional Materials*, in press.

[8] Iverson, B.D., Davis, T.W., Garimella, S.V., North, M.T. and Kang, S.S., 2007. Heat and mass transport in heat pipe wick structures. *Journal of Thermophysics and Heat Transfer*, 21(2), pp.392-404.

[9] Slobozhanin, L.A., Alexander, J.I.D., Collicott, S.H. and Gonzalez, S.R., 2006. Capillary pressure of a liquid in a layer of close-packed uniform spheres. *Physics of Fluids*, 18(8), p.082104. http://dx.doi.org/10.1063/1.2236123

[10] Prager, S., 1961. Viscous flow through porous media. *The Physics of Fluids*, 4(12), pp.1477-1482. http://dx.doi.org/10.1063/1.1706246

[11] Narayanan, S., Fedorov, A.G. and Joshi, Y.K., 2011. Interfacial transport of evaporating water confined in nanopores. *Langmuir*, 27(17), pp.10666-10676. https://doi.org/10.1021/la201807a

[12] Xiao, R., Maroo, S.C. and Wang, E.N., 2013. Negative pressures in nanoporous membranes for thin film evaporation. *Applied Physics Letters*, *102*(12), p.123103. http://dx.doi.org/10.1063/1.4798243

[13] Hanks, D.F., Lu, Z., Narayanan, S., Bagnall, K.R., Raj, R., Xiao, R., Enright, R. and Wang, E.N., 2014, May. Nanoporous evaporative device for advanced electronics thermal management. In *Thermal and Thermomechanical Phenomena in Electronic Systems (ITherm), 2014 IEEE Intersociety Conference on* (pp. 290-295). IEEE. https://doi.org/10.1109/ITHERM.2014.6892295

[14] Ćoso, D., Srinivasan, V., Lu, M.C., Chang, J.Y. and Majumdar, A., 2012. Enhanced heat transfer in biporous wicks in the thin liquid film evaporation and boiling regimes. *Journal of Heat Transfer*, *134*(10), p.101501. https://doi.org/10.1115/1.4006106

[15] Adera, S., Antao, D., Raj, R. and Wang, E.N., 2016. Design of micropillar wicks for thin-film evaporation. *International Journal of Heat and Mass Transfer*, 101, pp.280-294. https://doi.org/10.1016/j.ijheatmasstransfer.2016.04.107

[16] Narayanan, S., Fedorov, A.G. and Joshi, Y.K., 2010, June. Experimental characterization of a micro-scale thin film evaporative cooling device. In Thermal and Thermomechanical Phenomena in Electronic Systems (ITherm), *2010 12th IEEE Intersociety Conference* on (pp. 1-10). IEEE. https://doi.org/10.1109/ITHERM.2010.5501327

[17] Chang, J.Y. and You, S.M., 1997. Boiling heat transfer phenomena from microporous and porous surfaces in saturated FC-72. *International Journal of Heat and Mass Transfer*, 40(18), pp.4437-4447. https://doi.org/10.1016/S0017-9310(97)00055-0

[18] Li, C. and Peterson, G.P., 2007. Parametric study of pool boiling on horizontal highly conductive microporous coated surfaces. *Journal of heat transfer*, 129(11), pp.1465-1475. https://doi.org/doi:10.1115/1.2759969

[19] Lu, Z., Narayanan, S. and Wang, E.N., 2015. Modeling of evaporation from nanopores with nonequilibrium and nonlocal effects. *Langmuir*, 31(36), pp.9817-9824. https://doi.org/10.1021/acs.langmuir.5b01700

[20] Cai, S.Q. and Bhunia, A., 2014. Characterization of Phase Change Heat and Mass Transfers in Monoporous Silicon Wick Structures. *Journal of Heat Transfer*, 136(7), p.072001. https://doi.org/10.1115/1.4027152

[21] Bigham, S., Fazeli, A. and Moghaddam, S., 2017. Physics of microstructures enhancement of thin film evaporation heat transfer in microchannels flow boiling. *Scientific Reports*, *7*. http://dx.doi.org/10.1038/srep44745

[22] Hanlon, M.A. and Ma, H.B., 2003. Evaporation heat transfer in sintered porous media. *Transactions-American Society of Mechanical Engineers Journal of Heat Transfer*, 125(4), pp.644-652.

[23] Maroo, S.C. and Chung, J.N., 2011. Negative pressure characteristics of an evaporating meniscus at nanoscale. *Nanoscale research letters*, 6(1), p.72. https://doi.org/10.1186/1556-276X-6-72

[24] Wang, H., Garimella, S.V. and Murthy, J.Y., 2007. Characteristics of an evaporating thin film in a microchannel. *International journal of heat and mass transfer*, 50(19), pp.3933-3942.

[25] Lee, H., Mudawar, I. and Hasan, M.M., 2013. Flow condensation in horizontal tubes. *International Journal of Heat and Mass Transfer*, 66, pp.31-45. https://doi.org/10.1016/j.ijheatmasstransfer.2013.06.044

[26] Kharangate, C.R., Lee, H., Park, I. and Mudawar, I., 2016. Experimental and computational investigation of vertical upflow condensation in a circular tube. *International Journal of Heat and Mass Transfer*, 95, pp.249-263. https://doi.org/10.1016/j.ijheatmasstransfer.2015.11.010

[27] Lee, M.S., Aute, V., Riaz, A. and Radermacher, R., 2012. A review on direct two-phase, phase change flow simulation methods and their applications.

[28] Bodla, K.K., Murthy, J.Y. and Garimella, S.V., 2013. Evaporation analysis in sintered wick microstructures. *International Journal of Heat and Mass Transfer*, *61*, pp.729-741. https://doi.org/10.1016/j.ijheatmasstransfer.2013.02.038

[29] Ranjan, R., Murthy, J.Y. and Garimella, S.V., 2011. A microscale model for thin-film evaporation in capillary wick structures. *International Journal of Heat and Mass Transfer*, *54*(1), pp.169-179. https://doi.org/10.1016/j.ijheatmasstransfer.2010.09.037

[30] Ranjan, R., Murthy, J.Y. and Garimella, S.V., 2009. Analysis of the wicking and thin-film evaporation characteristics of microstructures. *Journal of Heat Transfer*, *131*(10), p.101001. https://doi.org/10.1115/1.3160538

[31] Mandel, R., Shooshtari, A. and Ohadi, M., 2017. Thin-film evaporation on microgrooved heatsinks. Numerical Heat Transfer, Part A: Applications, 71(2), pp.111-127. http://dx.doi.org/10.1080/10407782.2016.1257300

[32] Xu, X. and Carey, V.P., 1990. Film evaporation from a micro-grooved surface- an approximate heat transfer model and its comparison with experimental data. *Journal of Thermophysics and Heat Transfer*, *4*(4), pp.512-520. http://dx.doi.org/10.2514/3.215

[33] Stephan, P.C. and Busse, C.A., 1992. Analysis of the heat transfer coefficient of grooved heat pipe evaporator walls. *International Journal of heat and mass transfer*, *35*(2), pp.383-391. https://doi.org/10.1016/0017-9310(92)90276-X

[34] Ha, J.M. and Peterson, G.P., 1996. The interline heat transfer of evaporating thin films along a micro grooved surface. *Transactions-American Society of Mechanical Engineers Journal of Heat Transfer*, 118, pp.747-755.

[35] Ma, H.B. and Peterson, G.P., 1997. Temperature variation and heat transfer in triangular grooves with an evaporating film. *Journal of Thermophysics and Heat Transfer*, 11(1), pp.90-97.

[36] Weibel, J.A., Garimella, S.V. and North, M.T., 2010. Characterization of evaporation and boiling from sintered powder wicks fed by capillary action. *International Journal of Heat and Mass Transfer*, 53(19), pp.4204-4215. https://doi.org/10.1016/j.ijheatmasstransfer.2010.05.043

[37] Chen, Y., Melvin, L.S., Rodriguez, S., Bell, D. and Weislogel, M.M., 2009. Capillary driven flow in micro scale surface structures. *Microelectronic Engineering*, 86(4), pp.1317-1320. https://doi.org/10.1016/j.mee.2009.02.016

[38] Park, K., Noh, K.J. and Lee, K.S., 2003. Transport phenomena in the thin-film region of a micro-channel. *International Journal of Heat and Mass Transfer*, *46*(13), pp.2381-2388. https://doi.org/10.1016/S0017-9310(02)00541-0

[39] Wang, H., Garimella, S.V. and Murthy, J.Y., 2007. Characteristics of an evaporating thin film in a microchannel. *International journal of heat and mass transfer*, *50*(19), pp.3933-3942. https://doi.org/10.1016/j.ijheatmasstransfer.2007.01.052

[40] Wang, H., Murthy, J.Y. and Garimella, S.V., 2008. Transport from a volatile meniscus inside an open microtube. *International Journal of Heat and Mass Transfer*, *51*(11), pp.3007-3017. https://doi.org/10.1016/j.ijheatmasstransfer.2007.09.011

[41] Barako, M.T., Sood, A., Zhang, C., Wang, J., Kodama, T., Asheghi, M., Zheng, X., Braun, P.V. and Goodson, K.E., 2016. Quasi-ballistic Electronic Thermal Conduction in Metal Inverse Opals. *Nano letters*, 16(4), pp.2754-2761. http://dx.doi.org/10.1021/acs.nanolett.6b00468

[42] Pham, Q.N., Barako, M.T., Tice, J. and Won, Y., 2017. Microscale Liquid Transport in Polycrystalline Inverse Opals across Grain Boundaries. *Scientific Reports*, 7. http://dx.doi.org/10.1038/s41598-017-10791-3

[43] Brakke, K.A., 1992. The surface evolver. *Experimental mathematics*, 1(2), pp.141-165. http://dx.doi.org/10.1080/10586458.1992.10504253

[44] Schrage, R.W., 1953. A theoretical study of interphase mass transfer. *Columbia University Press*.

[45] Kharangate, C.R. and Mudawar, I., 2017. Review of computational studies on boiling and condensation. *International Journal of Heat and Mass Transfer*, 108, pp.1164-1196. https://doi.org/10.1016/j.ijheatmasstransfer.2016.12.065

[46] Marek, R. and Straub, J., 2001. Analysis of the evaporation coefficient and the condensation coefficient of water. *International Journal of Heat and Mass Transfer*, 44(1), pp.39-53. https://doi.org/10.1016/S0017-9310(00)00086-7

[47] Tanasawa, I., 1991. Advances in condensation heat transfer. *Advances in heat transfer*, 21, pp.55-139. https://doi.org/10.1016/S0065-2717(08)70334-4

[48] Patankar, S.V. and Spalding, D.B., 1972. A calculation procedure for heat, mass and momentum transfer in three-dimensional parabolic flows. *International journal of heat and mass transfer*, 15(10), pp.1787-1806. https://doi.org/10.1016/0017-9310(72)90054-3

[49] Peyret, R. ed., 1996. Handbook of computational fluid mechanics. *Academic Press*.

[50] Muzaferija, S., 1998. Computation of free surface flows using interface-tracking and interface-capturing methods. Nonlinear water wave interaction.

[51] Patankar, S., 1980. Numerical heat transfer and fluid flow. *CRC press*.

[52] Brackbill, J.U., Kothe, D.B. and Zemach, C., 1992. A continuum method for modeling surface tension. *Journal of computational physics*, 100(2), pp.335-354. https://doi.org/10.1016/0021-9991(92)90240-Y

[53] Schonberg, J.A. and Wayner, P.C., 1992. Analytical solution for the integral contact line evaporative heat sink. *Journal of thermophysics and heat transfer*, 6(1), pp.128-134.

[54] Park, K., Noh, K.J. and Lee, K.S., 2003. Transport phenomena in the thin-film region of a micro-channel. *International Journal of Heat and Mass Transfer*, 46(13), pp.2381-2388.

Supplementary Information

Microscopic Analysis of Thin-Film Evaporation on Spherical Pore Surfaces

Kimia Montazeri[1], Hyoungsoon Lee[2], Yoonjin Won[1*]

[1] *Mechanical and Aerospace Engineering, University of California, Irvine*
Irvine, CA 92697, USA
[2] *School of Mechanical Engineering, Chung-Ang University, South Korea*
** Corresponding author email: won@uci.edu*

1. Simulation Model Details

We list the details of simulation method in ANSYS Fluent to conduct computational fluidic dynamic calculations.

	Discretization scheme
Pressure-velocity coupling	SIMPLE
Volume fraction	Modified HRIC
Pressure	PRESTO!
Momentum	Second order upwind
Energy	Second order upwind
Wall adhesion	CSF

2. Thermophysical properties

We list the details of thermophysical properties of water and copper that we use in the simulation models in Table S2 and Table S3. In this table, the saturation temperature and enthalpy of evaporation are reported at P = 1 atm.

Table S2. Thermophysical properties of water

Properties	Units	Water
ρ	kg/m^3	998.2
c_p	J/kg×K	4182
μ	mPa s	1.003
M	kg/mol	0.018
T_{sat}	K	373.15
h_{fg}	kJ/kg	2256.39
k	W/m×K	0.6
R	J/mol×K	8.314

Table S3. Thermophysical properties of copper

Properties	Units	Copper
ρ	kg/m^3	8960
c_p	J/kg×K	385
k	W/m×K	400

3. Local Evaporative Mass Flux for Different Locations

The local evaporative mass flux is calculated based on the simplified Schrage model using Eq. (10). In this plot, evaporative mass flux is roughly inversely proportional to the corresponding local meniscus thickness, showing a maximum value at the wall where $r = r_{pore}$. Based on this, three main evaporation regimes can be identified as: high-evaporating regime, evaporating regime, and non-effective regime as a function of the radial location and their local values.

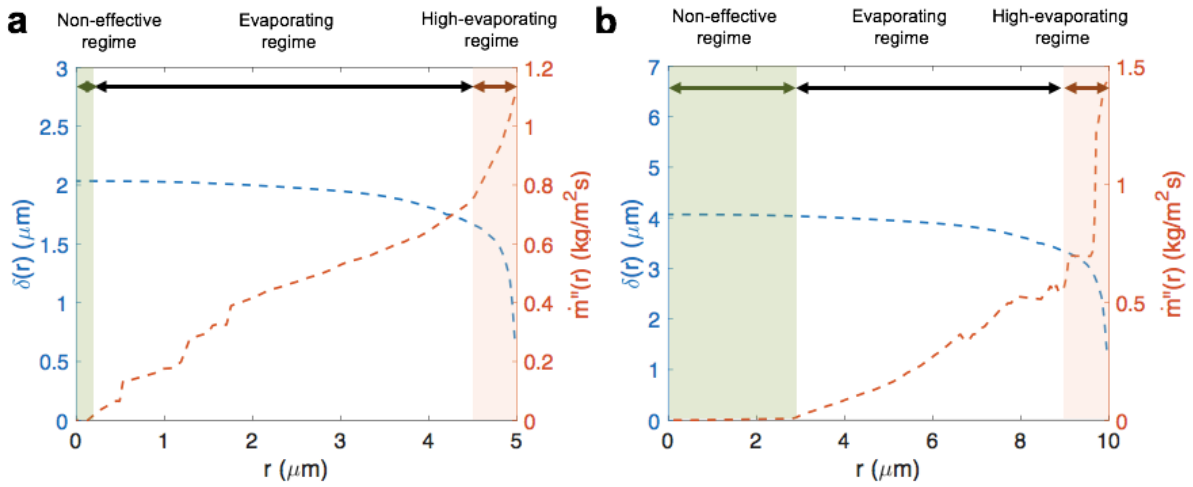

Figure S1. Local meniscus thickness and evaporative mass fluxes along the liquid-vapor interface (a) for the case of d_{pore} = 10 μm and (b) d_{pore} = 20 μm where the contact angle is 20°. Based on these local plots, the evaporation regimes are identified as high-evaporating regime, evaporating regime, and non-evaporating regime.

4. Area-averaged Evaporative Mass Flux for Different Cases

We perform a parametric study of evaporation performance by testing different pore diameters ranging from 10 to 20 μm. This range of pore diameter is selected based on the error analysis (See Section 6.2 for details). Area-averaged evaporative mass flux as a function of pore diameter and contact angles are plotted in Figure S2.

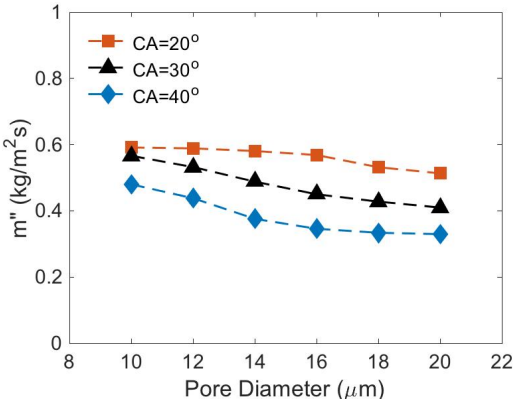

Figure S2. Area-averaged evaporation performance values for varying pore diameters and contact angles. Area-averaged evaporative mass flux is plotted for different cases. The changes in pore diameters and contact angles will significantly affect the corresponding heat transfer coefficients.

5. Mesh Independence Study

To confirm the independency of the results from the computational mesh of this work, we test three different mesh sizes by performing numerical simulation for each of them, as the details are listed in Table S4 and S5. Table S4 confirms the negligible differences between average T_{lv} and T_{sl} between different mesh sizes. In addition, the temperature deviation is calculated as the percentage ratio of the difference between the obtained T values at interfaces from each mesh and the mean T values of both meshes. Thereby, the calculation difference in percentage between mesh 1 and 2 as well as mesh 2 and 3 are calculated in Table S5.

Table S4. Detailed mesh information used for the mesh sensitivity study.

Mesh	Number of cells	Average Mesh Size	Average T_{lv}	Average T_{sl}
	number	μm	K	K
mesh 1	9151	0.112	374.780	376.492
mesh 2	36579	0.054	374.738	376.438
mesh 3	145019	0.024	374.714	376.352

Table S5. Calculation differences between different meshes

	Deviation for T_{lv} (%)	*Deviation for* T_{sl} (%)
Calculation difference between mesh 1 and 2	0.0011	0.014
Calculation difference between mesh 2 and 3	0.006	0.023

6. Simulation Validation Using Different Geometry

To validate the simulation method used in this study, the analysis methods analyze meniscus formation on cylindrical-shaped wires for one case [S1]. The diameter of the wires is 200 μm while the distance between two adjacent wires is 376 μm. Wires are initially superheated at 300.5 K, the vapor temperature is 298K, and the liquid inlet temperature is 298K. Contact angle is considered as 15°. VOF and Schrage models are applied to calculate temperature profiles (**Fig. S6(a)** and **(b)**) evaporation rates at the liquid-vapor interfaces. As a result, the evaporation rate is calculated as 0.33 kg/m^{2}s near the thin film region of the meniscus, which shows a very good agreement with the values reported by Ranjan (~0.5 kg/m^{2}s). The local heat transfer coefficient near the wall (0.87 μm < r < 0.96 μm) is calculated as 7.44×10^5 W/m^{2}K based on $h=q''/(T_{lv}-T_{sat})$, which is on the same order with the Ranjan's calculation.

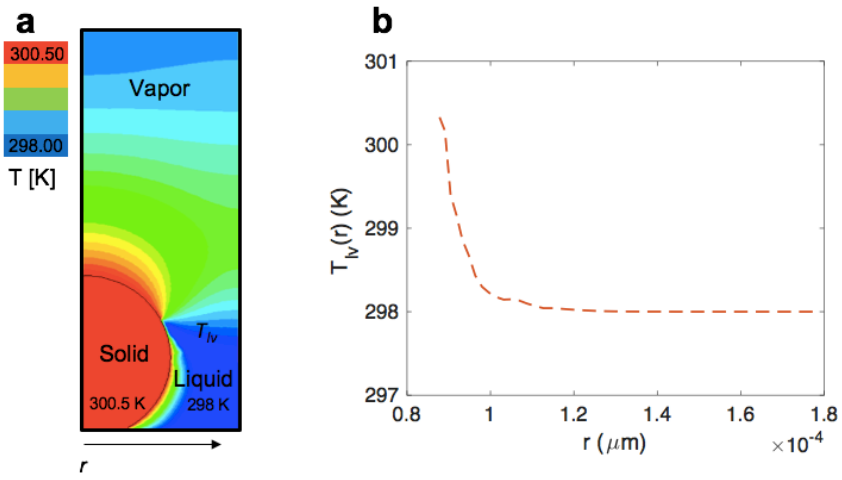

Figure S6 (1.5 columns). Temperature distribution between horizontal wires in 2D domain. (a) The diameter of the wires is 200 μm while the distance between two adjacent wires is 376 μm. The wire is initially superheated at 300.5 K, and the liquid inlet temperature is 298K from the bottom. (b) Temperature profile at the liquid and vapor interface is plotted.

References:

[S1] Ranjan, R., Murthy, J.Y. and Garimella, S.V., 2011. A microscale model for thin-film evaporation in capillary wick structures. *International Journal of Heat and Mass Transfer*, *54*(1), pp.169-179.
https://doi.org/10.1016/j.ijheatmasstransfer.2010.09.037